International Journal of Refractory Metals and Hard Materials 130 (2025) 107185

Contents lists available at ScienceDirect

International Journal of Refractory Metals and Hard Materials

journal homepage: www.elsevier.com/locate/IJRMHM

High-temperature oxidation of TiNbTaVW RHEA: Oxide layer formation under parabolic behaviour

Olufemi Sylvester Bamisaye [a,c,*], Nthabiseng Maledi [a,b], Desmond Klenam [a], Michael Oluwatosin Bodunrin [a,b]

[a] School of Chemical and Metallurgical Engineering, Faculty of Engineering and the Built Environment, University of the Witwatersrand, Johannesburg, South Africa
[b] DSI-NRF Centre of Excellence in Strong Materials, University of the Witwatersrand, Johannesburg, South Africa
[c] Mechanical Engineering Department, Faculty of Air Engineering, Air Force Institute of Technology, Kaduna, Nigeria

ARTICLE INFO

Keywords:
Surface morphology
Oxidation properties
Refractory high entropy alloy
High temperature materials

ABSTRACT

The potential of refractory high entropy alloys (RHEAs) as high-temperature structural materials depends on optimising their oxidation resistance. This study examines the surface and cross-sectional oxide layers of TiNbTaVW RHEA after five hours of oxidation, comparing them to previously studied layers formed after 15 h. At 850°C, the surface and cross-sectional oxide layers remained crack-free after 5 h, in contrast to the cracked layers observed after 15 h. A crack-free oxide layer effectively slows oxidation by limiting oxygen diffusion. However, at 1050°C, cracks were present in the surface and cross-sectional oxide layers after 5 h, similar to those observed after 15 h. Understanding short-term oxidation mechanisms provides valuable insights for developing strategies to enhance the high-temperature oxidation resistance of RHEAs.

1. Introduction

Oxidation resistance is essential for components that perform at high temperatures, as high-temperature oxidation can cause material degradation and failure. Understanding its mechanisms and enhancing the oxidation resistance of structural materials are essential for technical and economic benefits [1–4]. High-entropy alloys (HEAs) are a novel class of structural materials developed in 2004, based on multiple principal elements [5,6]. The HEA design approach benefits from high configurational entropy, enthalpy of mixing, sluggish diffusion, cocktail effects, and severe lattice distortions, which contribute to their exceptional mechanical properties, including high strength, hardness, wear resistance, corrosion resistance, and oxidation resistance [7–11]. The enhanced oxidation resistance observed in HEAs, such as in AlCoCrFeNi is attributed to sluggish diffusion effect and the formation of a duplex oxide structure consisting of a Cr-rich inner layer and an Fe-rich outer layer [12]. The outward diffusion of Al during oxidation in $Al_xCoCrFeNi$ HEAs may also be slowed down, further supporting the influence of sluggish diffusion on the oxidation mechanism [13]. Refractory high entropy alloys (RHEAs), introduced in 2010, are a subclass of HEAs composed primarily of refractory metals [14]. RHEAs are promising candidates for high-temperature structural materials due to their high hardness [14–19], oxidation resistance [20–23], wear resistance [24–29], corrosion resistance [30–34], and high temperature strength [35–42]. When exposed to oxidative environments, RHEAs can exhibit phenomena such as protective oxide layer formation, volatilisation, spallation and internal oxidation [43], making a clear understanding of their oxidation behaviour is important during their development.

Many studies have investigated the long-term oxidation behaviour of RHEAs [4,44–50]. Schellert et al. [47] observed a mass change of 6.19 mg/cm^2 in $TaMoCr_{10}TiAl$ RHEA at 1200°C after 24 h. Yan et al. [48] observed a mass gain of 31.83 mg/cm^2 in WTaNbTiAl RHEA at 1200°C after 48 h, attributing the oxidation resistance to $AlNbO_4$ and Ti-riched oxides that limit oxygen and cation diffusion. Zhu et al. [51] investigated the oxidation behaviour of $Ti_{1.5}NbVAl_{0.25}$, $Ti_{1.5}NbVAl_{0.5}$, $Ti_{1.5}NbVAl_{0.75}$ and $Ti_{1.5}NbVAl_1$ RHEAs at 800°C after 10 h and a mass gain of 31.71, 19.40, 11.84 and 8.26 mg/cm^2 was observed. Oxidation resistance was significantly improved with Al addition. Guo et al. [52] at 1000°C after 20 h found a mass gain of 61.7, 57.8 and 126.4 mg/cm^2 in oxidised $TaMo_{0.5}NbZrTi_{1.5}Al_{0.1}$, $TaMo_{0.5}NbZrTi_{1.5}Al_{0.1}Si_{0.1}$ and $TaMo0_{.5}ZrTi_{1.5}Al_{0.1}Si_{0.2}$ RHEAs.

Apart from long-term oxidation conditions, short-term oxidation is

* Corresponding author at: School of Chemical and Metallurgical Engineering, Faculty of Engineering and the Built Environment, University of the Witwatersrand, Johannesburg, South Africa.
E-mail address: 2503285@students.wits.ac.za (O.S. Bamisaye).

https://doi.org/10.1016/j.ijrmhm.2025.107185
Received 7 December 2024; Received in revised form 1 March 2025; Accepted 8 April 2025
Available online 9 April 2025

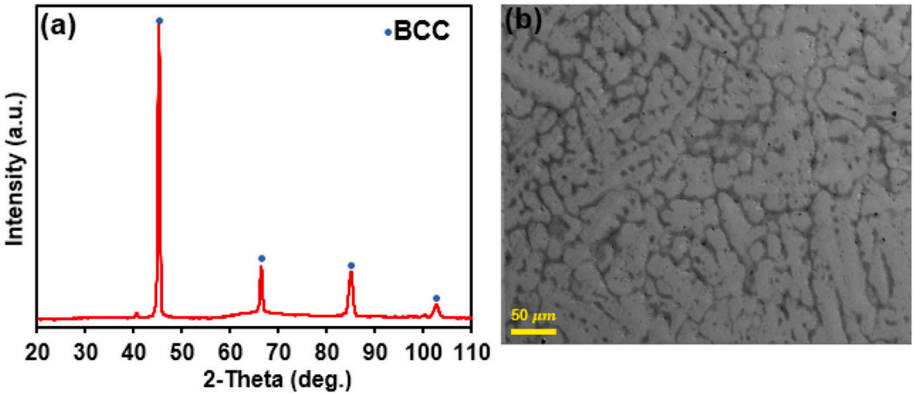

Fig. 1. XRD pattern of the phase present in the TiNbTaVW RHEA (a); SEM-BSE image of the TiNbTaVW RHEA (b) (Reproduced with permission. [58] Copyright 2024, The Authors, published by Elsevier B.V.)

another possible high-temperature oxidation situation [47,53–56]. Waseem and Ryu [56] found the mass gain of $Al_{10}CrMo_0NbTiZr_{10}$, $Al_{10}CrMo_4NbTiZr_{10}$ and $Al_{10}CrMo_8NbTiZr_{10}$ RHEAs to be 1.09, 2.01 and 3.05 mg/cm^2 at 1000 °C after 1 h. The lower mass gain of $Al_{10}CrMo_0NbTiZr_{10}$ was attributed to the protective oxides of Al_2O_3 and $CrNbO_4$. Shangguan et al. [57] investigated the oxidation performance of TiZrHfNbTaV RHEA at 800–1000 °C after 1 h and a brittle-like (Hf, Zr)O_2 formed in the RHEA, which caused pores in the oxide layers and served as rapid oxygen ingress to the substrate. Sheikh et al. [54] studied the oxidation resistance of $Al_{0.5}Cr_{0.25}Nb_{0.5}Ta_{0.5}Ti_{1.5}$, $Al_{0.75}Cr_{0.25}Nb_{0.5}Ta_{0.5}Ti_{1.5}$ and $Al_{0.5}Cr_{0.25}Nb_{0.5}Ta_{0.5}Ti_{1.5}Zr_{0.01}$ RHEAs at 800 °C after 1 h. The outer layers of all the RHEAs are partly oxidised and internal oxidation was observed. It was also found that the $Al_{0.75}Cr_{0.25}Nb_{0.5}Ta_{0.5}Ti_{1.5}$ RHEA has the lowest oxygen dissolution, confirming that the formed oxide layer is effective in controlling the oxygen adsorption into the substrate. Zhang et al. [55] studied the oxidation resistance properties of $Al_1CrTiMo$, $Al_{0.75}CrTiMo$, $Al_{0.5}CrTiMo$ and $Al_{0.25}CrTiMo$ RHEAs at 1000 °C after 7 h and found the mass gain to be 12.21 mg/cm^2, 9.34 mg/cm^2, 5.58 mg/cm^2 and 3.58 mg/cm^2. The oxidation resistance was significantly improved with lower Al addition. A previously developed TiNbTaVW RHEA exhibited higher temperature strength and hardness, excellent corrosion resistance but exhibited mass loss when exposed to oxidation after 15 h at 850°C and 1050°C [58]. However, a parabolic curve was observed up to two oxidation cycles [58]. A parabolic curve indicates a diffusion-controlled process in which the diffusion of oxygen through the oxide layer to the oxide/substrate interface is the rate-limiting oxidation process [59,60].

Therefore, it is crucial to investigate the surface and cross-sectional oxide layers formed on TiNbTaVW RHEA during parabolic oxidation behaviour. The characteristics of the surface and cross-sectional oxide layers were analysed at 850°C and 1050°C for 5 h and compared to previously reported oxide layers formed after 15 h [58]. The oxidation mechanisms at 850°C and 1050°C after 5 h were also discussed. An understanding of the oxidation mechanisms will be helpful in designing RHEAs with excellent oxidation resistance.

2. Experimental procedure

The TiNbTaVW RHEA was produced through vacuum arc melting under ultra-high-purity argon gas on a water-cooled copper hearth to obtain an arc-melted alloy. TiNbTaVW was synthesised using commercial high-purity elemental powders of Ti (99.7 wt% purity), Nb (99.9 wt % purity), V (99.9 wt% purity), Ta (99.95 wt% purity), and W (99.9 wt% purity) supplied by Weartech (Pty) Limited, South Africa. *To ensure* chemical homogeneity, the TiNbTaVW sample was flipped and remelted three times. The TiNbTaVW sample was then sectioned into nominal dimensions of 7.0 × 7.0 × 6.0 mm^3 using a Gold San CNC wire-cutting EDM machine for cyclic oxidation tests. The sample surfaces were ground using P1200 SiC paper, cleaned ultrasonically in acetone, and air-dried. The oxidation temperatures were selected based on accelerated oxidation already reported in some RHEAs (700°C–850°C) [7,20,23,61,62] and high-temperature effects (>1000°C) [4,7,63–65], while the oxidation time was based on the parabolic oxidation behaviour of TiNbTaVW RHEA [58]. Cyclic oxidation tests were performed in a muffle furnace under static air at 850°C and 1050°C for 5 h at a heating rate of 10°C/min. The first hour of oxidation was dedicated to assessing the initial integrity of the oxide layer after cooling. Subsequently, each cycle consisted of 2 h of heating at the specified furnace temperatures, followed by 20 min of air cooling at room temperature.

Table 1
Composition distribution of the TiNbTaVW RHEA (at. %) (Reproduced with permission. [58] Copyright 2024, The Authors, published by Elsevier B.V.)

	Element	Ti	Nb	Ta	V	W
TiNbTaVW RHEA	Actual	19 ± 0.4	20 ± 0.2	21 ± 0.2	20 ± 0.3	20 ± 0.2
	Dendrite (grey)	14 ± 0.8	19 ± 0.5	24 ± 0.5	15 ± 1.1	28 ± 1.9
	Interdendrite (dark)	32 ± 1.5	19 ± 0.3	12 ± 0.8	29 ± 0.6	8.0 ± 1.0

The microstructure of the oxidised samples, including surface and cross-sectional features, was analysed using a field emission gun-scanning electron microscope (FEG-SEM) equipped with secondary electron (SE) and back-scattered electron (BSE) detectors at 20 kV. The oxides formed during oxidation were identified using a Bruker D2 phase diffractometer with a Co Kα radiation source [λ = 1.78899 Å] at 30 kV and 25 mA within a 2θ range of 20 to 90° at 25°C. Oxide layers estimate was performed using Image J, an open-source software developed by National Institutes of Health.

3. Results

3.1. Phase and microstructure of the TiNbTaVW RHEA

The phase and microstructure of the TiNbTaVW RHEA is presented in Fig. 1 and is reproduced from previous work [58]. In Fig. 1a, the X-ray diffraction (XRD) analysis result of the TiNbTaVW RHEA shows peaks indexed as the BCC solid solution phase (Im-3 m (229); a = b = c = 3.2350 Å), observed within a wide range of 2θ values between 46° and 103°. The SEM-BSE image of the TiNbTaVW RHEA exhibits a dendritic microstructure (Fig. 1b). The elemental composition of TiNbTaVW is presented in Table 1 and is reproduced from previous work [58].

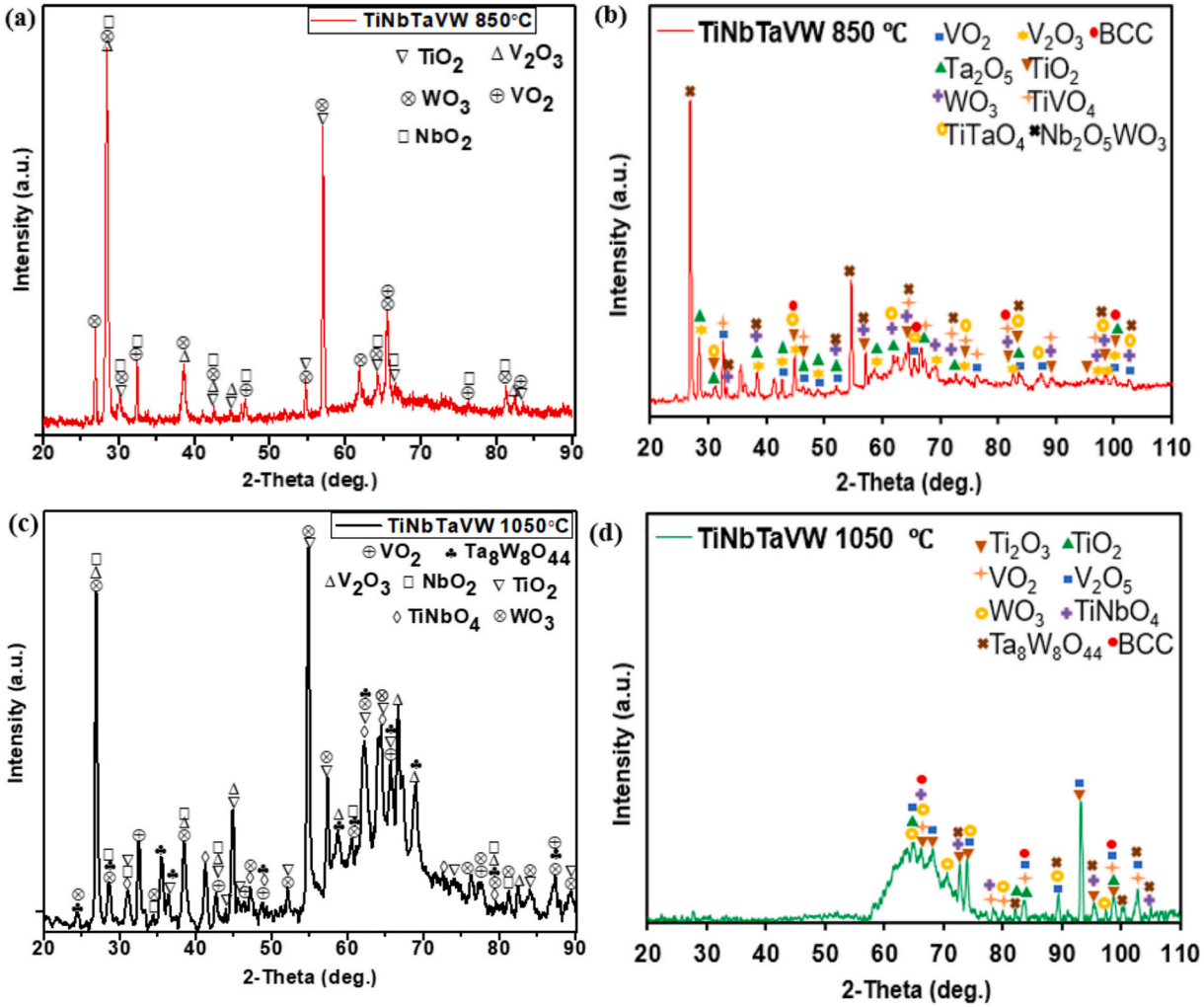

Fig. 2. XRD patterns of identified oxides in the TiNbTaVW RHEA at 850 °C after 5 h (a) and 15 h (b) (Reproduced with permission. [58] Copyright 2024, The Authors, published by Elsevier B.V.); and at 1050 °C after 5 h (c) and 15 h (d) (Reproduced with permission. [58] Copyright 2024, The Authors, published by Elsevier B.V.).

3.2. Oxidation analysis

3.2.1. Phase analysis and surface morphologies of the oxidised TiNbTaVW

The XRD patterns of the oxidised TiNbTaVW RHEA at 850 °C and 1050 °C after 5 h as compared to 15 h are shown in Fig. 2. The identified oxides of the TiNbTaVW RHEA at 850 °C after 5 h were VO_2, V_2O_3, TiO_2, NbO_2 and WO_3 (Fig. 2a). When compared with the identified oxides at 850 °C after 15 h (Fig. 2b) [58], Ta_2O_5, $TiVO_4$, $TiTaO_4$ and $Nb_2O_5WO_3$ were not observed after 5 h (Fig. 2a). At 1050 °C after 5 h, oxides of $TiNbO_4$ and $Ta_8W_8O_{44}$ were found with the already identified oxides at 850 °C after 5 h (Fig. 2c). The identified oxides (TiO_2, VO_2, WO_3, $TiNbO_4$ and $Ta_8W_8O_{44}$) at 1050 °C after 5 h were also observed after 15 h (Fig. 2d) [58].

The SEM images of the surface oxide layer of the TiNbTaVW RHEA at 850°C after 5 h and 15 h are presented in Fig. 3 [58]. After 5 h, the surface oxide layer displayed spalled Ti-rich oxide particles (Fig. 3a and Supporting Information S1), while W-rich oxide particles were observed after 15 h (Fig. 3b) [58]. It was also found that a surface oxide layer without cracks and pores was observed after 5 h, compared to the cracks and pores observed after 15 h (Fig. 3b). A crack-free and stable surface layer limit oxygen diffusion through the oxide layer [66]. At higher magnification, the surface scale layer after 5 h revealed rod-shaped oxides distributed across the surface (Fig. 3c), whereas the oxide layer after 15 h consisted of both rod-shaped and granular oxides (Fig. 3d) [58]. Similar rod-shaped oxides have been observed in other oxidised RHEAs, such as NbMoTaW [67], TiC/WMoTaNbV [68], $TiZrV_{0.5}Nb_{0.5}$ [69], TiZrHfNbTaV [57] and CrMoNbTaV [70]. The rod-shaped oxides observed after 5 h were mostly NbTiTaVW-rich (Supporting Information S2), whereas those observed after 15 h were mainly NbTaWV-rich [58].

The SEM images of the surface oxide layer of the TiNbTaVW RHEA at 1050 °C after 5 h and 15 h are shown in Fig. 4. A spalled surface oxide layer with cracks was observed after 5 h. A spalled Ti-rich oxides was found in several regions of the surface oxide layer (Fig. 4a and Supporting Information S3). These features were comparable to those observed after 15 h, with the presence of cracks and Ti-rich spalled oxides (Fig. 4b) [58]. At higher magnification, the surface oxide layer after 5 h revealed rod-shaped oxides distributed across the surface (Fig. 4c), while the oxide layer after 15 h comprised both granular-shaped and rod-shaped oxides after 15 h (Fig. 4d) [58]. The rod-shaped oxides observed at 1050°C after 5 h were mostly NbTiTaVW-rich oxides (Supplementary Information S4).

3.2.2. Cross-section analysis of the oxidised TiNbTaVW

The adhesion of the oxide layer to the metallic substrate is influenced by several factors, including scale thickness, growth rate, stress state, interfacial energy, and the elastic properties of the oxide [71]. The cross-sectional layer of the oxidised TiNbTaVW at 850 °C and 1050 °C after 5 h and 15 h [58] are shown in Fig. 5. At 850 °C after 5 h, a 139 ± 2.4 μm

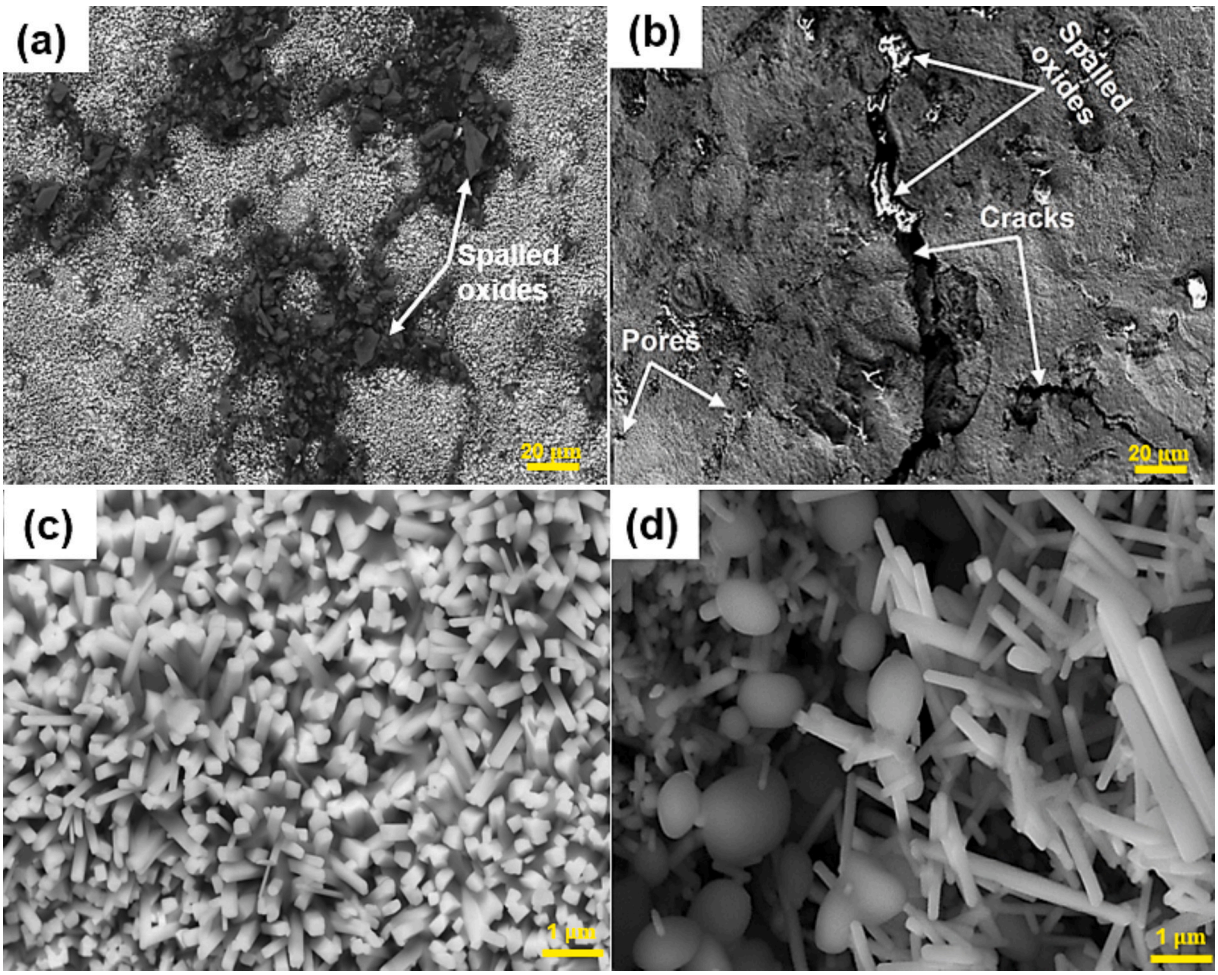

Fig. 3. SEM-BSE images of the surface oxide layer of TiNbTaVW RHEA at 850°C. (a) Compact surface containing spalled oxides after 5 h; (b) Cracks, pores, and spalled oxides after 15 h (Reproduced with permission. [58] Copyright 2024, The Authors, published by Elsevier B.V.); (c) Rod-shaped oxides after 5 h; (d) Granular and rod-shaped oxides after 15 h (Reproduced with permission. [58] Copyright 2024, The Authors, published by Elsevier B.V.).

thick oxidised layer and internal oxidation region were observed (Fig. 5a), compared to a 368 ± 1.1 μm thick oxidised layer with cracks after 15 h (Fig. 5b) [58]. The absence of cracks in the cross-sectional oxide layer after 5 h effectively prevented direct oxygen ingress into the oxide layer and metallic substrate, thereby reducing the oxidation rate. The oxide layer served as a reliable diffusion barrier, isolating the substrate from oxygen and reducing oxidation [7]. EDS analysis at 850 °C after 5 h revealed WTaNbVTi-rich oxides in the thick oxide layer and VTiTaNbW-rich oxides in the internal oxidation zone (Supplementary Information S5). After 15 h, the oxide layer exhibited similar NbTaWV-rich compositions, while VTiNb-rich oxides were detected in the internal oxidation zone [58].

At 1050°C after 5 h, a 227 ± 2.1 μm thick oxidised layer and internal oxidation region with cracks were observed (Fig. 5c). Similarly, a 375 ± 3.7 μm thick oxidised layer with cracks was found after 15 h (Fig. 5d) [58]. The cracks in the oxide layer are attributed to the metallic substrate contracting more rapidly than the oxide during cooling, resulting in compressive stresses that are released as cracks [72]. The EDS analysis of the thick oxide layer at 1050°C after 5 h revealed WTaNbTiV-rich oxides, consistent with WTaNb-rich oxides observed at 850 °C after 5 h. However, the internal oxidation zone mostly contained VTi-rich oxides (Supplementary Information S6). The oxide layer of TiNbTaVW RHEA at 1050°C after 15 h contained VNbWTa-rich oxides [58], similar to those obtained after 5 h. The internal oxidation zone exhibited compositions of TiVNbW-rich oxides after 15 h [58].

4. Discussion

Oxide growth is controlled by the inward diffusion of oxygen and the outward diffusion of metal atoms through the primary oxide layer. A schematic of the oxidation mechanisms of the TiNbTaVW RHEA at 850 °C and 1050 °C after 5 h is shown in Fig. 6. Oxygen dissolution into the RHEA leads to oxide formation: VO_2, V_2O_3, WO_3, TiO_2, NbO_2, $TiNbO_4$ and $Ta_8W_8O_{44}$ (Fig. 6a and b).

The standard free energy ($\triangle G_f$: kJ mol^{-1}) of simple oxides observed has been reported [48,73–77]. At 850°C, the stability and possible sequence of oxide formation is TiO_2 (−743) > NbO_2 (−644) > V_2O_3 (−639) > VO_2 (−521) > WO_3 (−384). At 1050°C, the order is TiO_2 (−710) > NbO_2 (−604) > V_2O_3 (−602) > VO_2 (−467) > WO_3 (−346). Among the simple oxides formed, WO_3 had the largest free energy, making it the least stable oxide on the surface of TiNbTaVW at both temperatures after 5 h. Additionally, TiO_2 had the smallest free energy, making it the most stable oxide on the surface of TiNbTaVW at both temperatures after 5 h. The reactions involved in the formation of the oxides at 850 °C and 1050 °C after 5 h are represented in Eqs. (1) to (7).

$$V(s) + O_2(g) \rightarrow VO_2(s) \quad (1)$$

$$Ti(s) + O_2(g) \rightarrow TiO_2(s) \quad (2)$$

$$4\,V(s) + 3O_2(g) \rightarrow 2V_2O_3(s) \quad (3)$$

$$2WO_2(s) + O_2(g) \rightarrow 2WO_3(s) \quad (4)$$

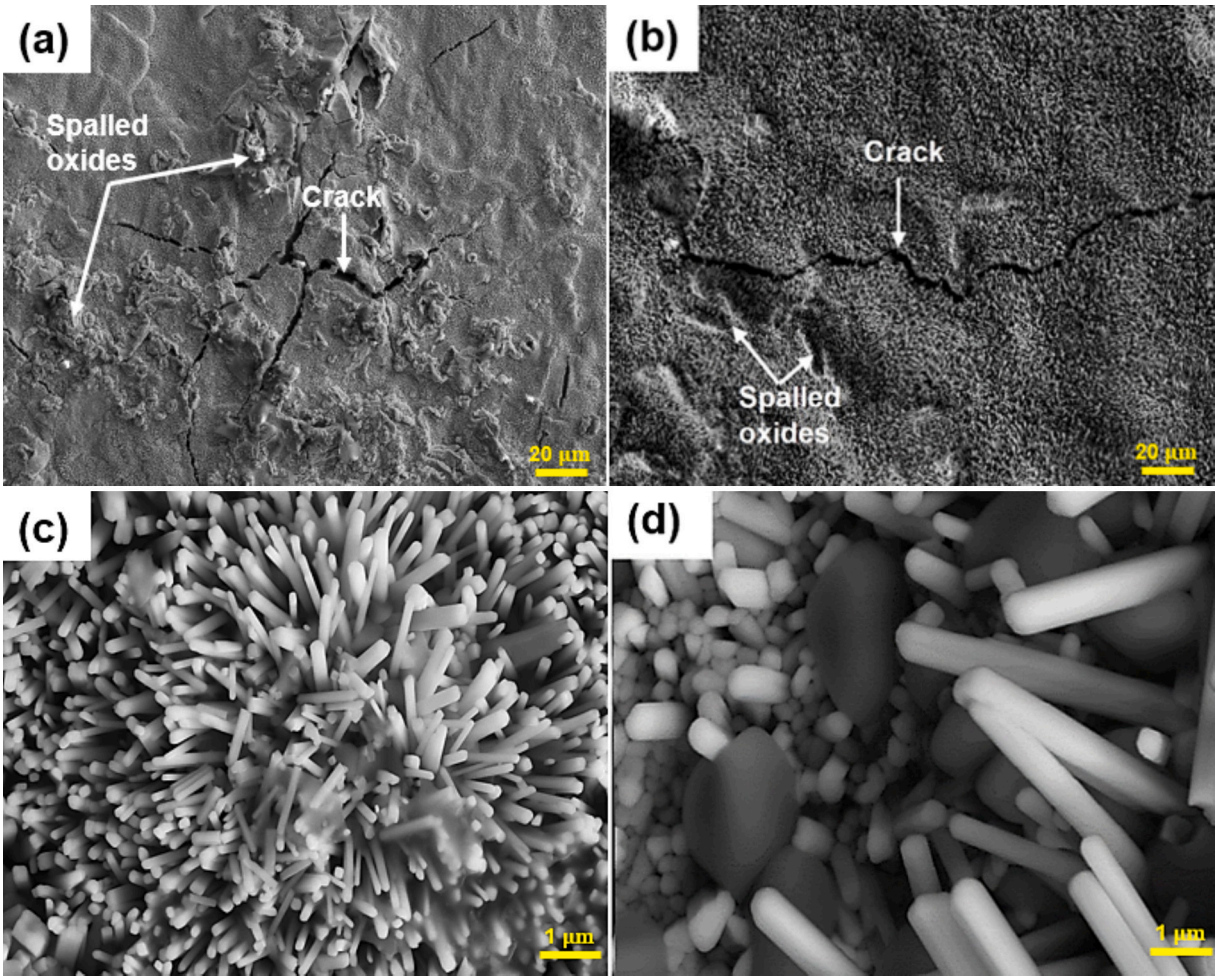

Fig. 4. SEM-BSE images of surface oxide layer of TiNbTaVW RHEA at 1050 °C. (a) Spalled surface, spalled Ti-rich oxides and cracks after 5 h; (b) Cracks and spalled Ti-rich oxides after 15 h (Reproduced with permission. [58] Copyright 2024, The Authors, published by Elsevier B.V.); (c) Rod-shaped oxides after 5 h; (d) Granular and rod-shaped oxides after 15 h (Reproduced with permission. [58] Copyright 2024, The Authors, published by Elsevier B.V.).

$$Nb(s) + O_2(g) \rightarrow NbO_2(s) \quad (5)$$

$$8WO_3(s) + 4Ta_2O_5(s) \rightarrow Ta_8W_8O_{44}(s) \quad (6)$$

$$TiO_2(s) + NbO_2(s) \rightarrow TiNbO_4(s) \quad (7)$$

The formation of simple oxides created a protective continuous layer at 850°C after 5 h. These oxides formed a protective barrier for both the inward and outward diffusion of oxygen, which eventually slowed down oxidation (Fig. 6a). This is evidenced in Figs. 3a and 5a, where no pores and cracks were observed. This allowed the growth of the oxides and oxide scale to be slower due to controlled oxygen diffusion, as compared to the rapid growth and thickening of the oxides after 15 h (Fig. 3d) [58]. Furthermore, the EDS analysis of the substrate shows a lower trend in oxygen dissolution (Fig. S7). It was also evident that the substrate retained the same dendritic structure (Fig. 5). The dendrite region are more W and Ta concentrated, while interdendrite region are more Ti and V concentrated. A small amount of oxygen was dissolved in both the dendrite and interdendrite regions after 5 h of oxidation, indicating slight oxidation in the substrate that was insufficient to cause cracking (Fig. S6). Significant oxygen diffusion into the substrate could initiate intergranular oxidation [78]. If oxygen reaches the grain boundary migration zone and a non-compact oxide form, cracks may develop in the highly oxidised region [78,79]. TiO_2 is a thermodynamically stable oxide that forms an adherent layer, providing good oxidation resistance and resulting in lower mass gains [48,77,80]. TiO_2 protects alloy surfaces by preventing continuous oxygen diffusion into the alloy matrix [24]. Hence, the oxide scales at 850 °C after 5 h are well protected and adhered to the alloy matrix.

Cracks and spalled surface oxide layer were observed in TiNbTaVW at 1050 °C after 5 h as shown in Figs. 4a, 5c and 6b. The compactness of oxide layers decreases during oxidation due to partial peeling, exposing the alloy surface to further oxidation [24]. Oxide growth during oxidation and different thermal expansions between the oxides and the metal during cooling contribute to cracking, pores, and voids [17,58,81,82]. In cyclic oxidation, the oxide scale grows via diffusion during heating, spalls during cooling, and regrows upon reheating [83,84]. Cooling creates compressive stresses and shear cracks as the metal substrate contracts faster than the oxide layer [72]. The Pilling-Bedworth ratio (PBR) defines the volume difference between the oxide and the metal forming the oxide of the identified oxides [82]. The identified PBR for simple oxides of TiO_2, VO_2, V_2O_3, WO_3 and NbO_2 were 1.77, 2.17, 1.84, 3.39 and 1.95. The PBRs for VO_2 and WO_3 are greater than 2, indicating high stress between oxides and the matrix, which easily leads to the formation of cracks observed in TiNbTaVW at 1050 °C after 5 h (Fig. 6b).

The high stress between oxides and the matrix due to high PBRs of VO_2 and WO_3 has also been observed in TiNbTaVW at 1050°C after 15 h [58]. Also, the growth of the oxides and oxide scale is thicker due to fast oxygen diffusion at 1050°C after 5 h (Figs. 4c and 5c), as compared to the slow growth and thinness of the oxide scale at 850 °C after 5 h (Figs. 3c and 5a). Although the PBRs for VO_2 and WO_3 are greater than

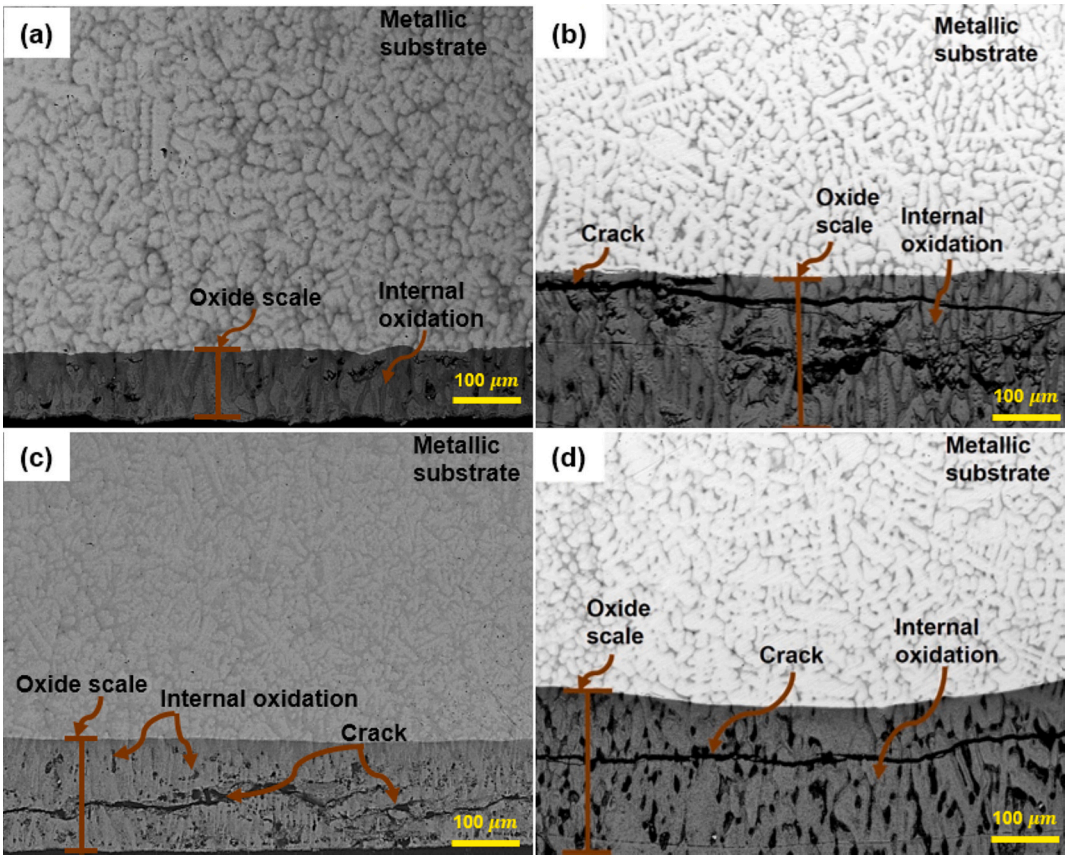

Fig. 5. SEM-BSE images of cross-sectional morphology of TiNbTaVW RHEA at 850°C after 5 h (a) and (b) after 15 h (b) (Reproduced with permission. [58] Copyright 2024, The Authors, published by Elsevier B.V.); SEM-BSE images of the TiNbTaVW RHEA's cross-sectional morphology at 1050 °C after 5 h (c) and (d) after 15 h (Reproduced with permission. [58] Copyright 2024, The Authors, published by Elsevier B.V.).

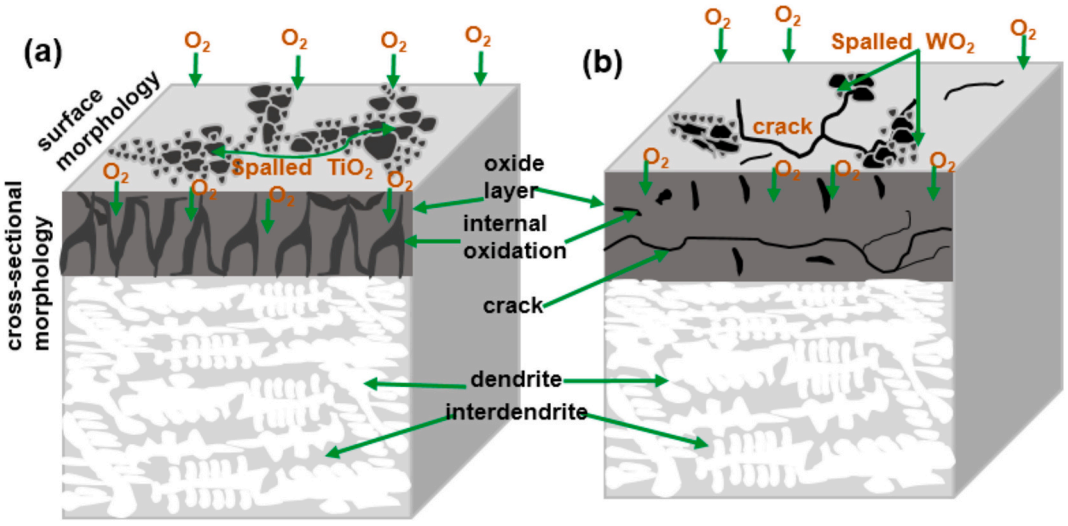

Fig. 6. Schematic of the TiNbTaVW RHEA oxidation mechanism at 850°C after 5 h (a) and 1050°C after 5 h (b).

2, defect formation was not observed at 850°C after 5 h because volume expansion between the metal and the oxide layer interface was well controlled during heating and cooling. The high thermal oxidation resistance of a metallic material is provided by a protective TiO_2 scale [85,86]. However, this scale becomes unstable at temperatures above 900°C due to the formation of volatile or non-protective oxides [85,86].

At 1050°C, TiO_2 reacts with NbO_2 to form $TiNbO_4$ and could be ineffective at providing protection, as evidenced by cracks at the oxide layers. The volatile nature of WO_3 due to its low sublimation temperature leads to its reaction with Ta_2O_5 [87] and Nb_2O_5 to form complex oxides such as $Ta_8W_9O_{47}$ and $Nb_8W_9O_{47}$ [48], which are ineffective in protecting the substrate [48]. The $Ta_8W_8O_{44}$ was found at 5 and 15 h at 1050 °C in the TiNbTaVW RHEA. The formed $Ta_8W_8O_{44}$ oxide at 1050 °C after 5 h was ineffective in protecting the TiNbTaVW RHEA. VO_2 and V_2O_5 oxides hinder the formation of protective scales and facilitate crack nucleation, significantly impacting oxidation resistance

[70,73,88]. VO_2 was observed at 850°C and 1050°C after 5 h, which could hinder the formation of protective oxides and facilitate the nucleation of cracks in TiNbTaVW at 1050°C.

The EDS analysis of the substrate indicates a lower trend in oxygen dissolution (Fig. S8), similar to that observed in the substrate at 850°C. Furthermore, the substrate retained its dendritic structure (Fig. 5), with the dendrite regions enriched in W and Ta, while the interdendrite regions are enriched in Ti and V. Similar to oxygen diffusion at 850°C, only a small amount of oxygen was detected in both the dendrite and interdendrite regions, suggesting minimal oxidation within the substrate, insufficient to induce intergranular oxidation that could lead to cracking (Fig. S7). This indicates that the observed cracks and spallation in the surface oxide layer developed during air cooling to room temperature due to thermal stresses i.e., the mismatch in coefficient of thermal expansion between the surface oxides and the substrate [17,24,58,81,82]. Oxygen enrichment on an alloy's oxide layer is closely related to oxide cracking, as oxygen dissolution increases lattice constants and, consequently, the oxides' volumetric expansion [53]. It was also observed that the cracks did not penetrate the substrate but remained confined to the cross-sectional oxide layer (Fig. 5c). This suggests that the cracks in the cross-sectional oxide layer developed during air cooling to room temperature due to thermal stresses, specifically the mismatch in the coefficient of thermal expansion between the oxygen enriched cross-sectional oxide layer and the substrate [8,44,49,59,66,67].

5. Conclusions

The surface and cross-sectional oxide layers of TiNbTaVW RHEA after five hours of oxidation was investigated and compared to its previously reported oxide layers after 15 h. The key findings from this study are as follows:

- At 850°C, simple oxides (TiO_2, V_2O_3, WO_3, VO_2, NbO_2) formed after 5 h, while both simple and complex oxides ($TiVO_4$, $TiTaO_4$, $Nb_2O_5WO_3$) appeared after 15 h. At 1050°C, complex oxides like $TiNbO_4$ and $Ta_8W_8O_{44}$ were observed were observed alongside simple oxides after 5 and 15 h.
- At 850°C after 5 h of oxidation, the surface oxide layer remained free of cracks and pores, whereas after 15 h, cracks and pores were observed. In contrast, at 1050°C, cracks were present in the surface oxide layers after both 5 and 15 h of oxidation.
- The surface oxide structure after 5 h comprises rod-shaped oxides when compared with rod-shaped and granular-shaped oxides after 15 h at 850°C. Rod-shaped oxides were still found at 1050°C after 5 h as compared with rod-shaped and granular-shaped oxides after 15 h.
- At 850°C, the TiNbTaVW RHEA cross-sectional oxide layer is 139 ± 2.4 μm thick after 5 h without cracks as compared to the 368 ± 1.1 μm with cracks after 15 h. At 1050°C, the cross-sectional oxide layer is 227 ± 2.1 μm thick with cracks after 5 h as compared to 375 ± 3.7 μm after 15 h.
- At 850°C after 5 h, crack-free oxide layers slow oxidation by preventing oxygen diffusion, while cracks in the oxide layer at 1050°C developed during cooling due to volume expansion between the substrate and the oxide layer.

CRediT authorship contribution statement

Olufemi Sylvester Bamisaye: Writing – original draft, Visualization, Validation, Software, Methodology, Investigation, Formal analysis, Data curation, Conceptualization. **Nthabiseng Maledi:** Writing – review & editing, Visualization, Validation, Supervision, Resources, Project administration, Methodology, Investigation, Funding acquisition, Conceptualization. **Desmond Klenam:** Writing – review & editing, Visualization, Software. **Michael Oluwatosin Bodunrin:** Writing – review & editing, Visualization, Validation, Supervision, Software, Resources, Project administration, Methodology, Investigation, Funding acquisition, Conceptualization.

Declaration of competing interest

The authors declare that they have no known competing financial interests or personal relationships that could have appeared to influence the work reported in this paper.

Appendix A. Supplementary data

Supplementary data to this article can be found online at https://doi.org/10.1016/j.ijrmhm.2025.107185.

Data availability

Data will be made available on request.

References

[1] O.N. Senkov, S.V. Senkova, D.M. Dimiduk, C. Woodward, D.B. Miracle, Oxidation behavior of a refractory $NbCrMo_{0.5}Ta_{0.5}TiZr$ alloy, J. Mater. Sci. 47 (2012) 6522–6534, https://doi.org/10.1007/s10853-012-6582-0.
[2] O.N. Senkov, J. Gild, T.M. Butler, Microstructure, mechanical properties and oxidation behavior of NbTaTi and NbTaZr refractory alloys, J. Alloys Compd. 862 (2021) 158003, https://doi.org/10.1016/j.jallcom.2020.158003.
[3] F. Müller, B. Gorr, H. Christ, H. Chen, M. Heilmaier, F. Müller, B. Gorr, H. Christ, H. Chen, Materials at high temperatures effect of microalloying with silicon on high temperature oxidation resistance of novel refractory high-entropy alloy ta-Mo-Cr-Ti-Al, Mater. High Temp. 3409 (2018) 1389115, https://doi.org/10.1080/09603409.2017.1389115.
[4] F. Müller, B. Gorr, H.J. Christ, H. Chen, A. Kauffmann, M. Heilmaier, Effect of Y additions on the oxidation behaviour of novel refractory high-entropy alloy NbMoCrTiAl at 1000 °C in air, Oxid. Met. 94 (2020) 147–163, https://doi.org/10.1007/s11085-020-09983-6.
[5] B. Cantor, I.T.H. Chang, P. Knight, A.J.B. Vincent, Microstructural development in equiatomic multicomponent alloys, Mater. Sci. Eng. A 375–377 (2004) 213–218, https://doi.org/10.1016/j.msea.2003.10.257.
[6] J.W. Yeh, S.K. Chen, S.J. Lin, J.Y. Gan, T.S. Chin, T.T. Shun, C.H. Tsau, S.Y. Chang, Nanostructured high-entropy alloys with multiple principal elements: novel alloy design concepts and outcomes, Adv. Eng. Mater. 6 (2004) 299–303, https://doi.org/10.1002/adem.200300567.
[7] B. Gorr, F. Müller, M. Azim, H.J. Christ, T. Müller, H. Chen, A. Kauffmann, M. Heilmaier, High-temperature oxidation behavior of refractory high-entropy alloys: effect of alloy composition, Oxid. Met. 88 (2017) 339–349, https://doi.org/10.1007/s11085-016-9696-y.
[8] F. Ceritbinmez, A. Günen, M.A. Akhtar, K. Patel, S. Mukherjee, L. Yünlü, E. Kanca, Surface integrity characteristics in wire-EDM of HfTaTiVZr refractory high entropy alloy, Adv. Mater. Process. Technol. 9 (2022) 1683–1700, https://doi.org/10.1080/2374068X.2022.2130869.
[9] F. Ceritbinmez, E. Kanca, L. Yünlü, K. Patel, M.A. Akhtar, S. Mukherjee, A. Günen, Wire electric discharge machining and its effect on the surface finish of HfNbTaTiZr refractory high-entropy alloy, Int. J. Adv. Manuf. Technol. 125 (2023) 1419–1427, https://doi.org/10.1007/s00170-022-10797-w.
[10] M.C. Gao, Progress in high-entropy alloys, JOM 66 (2014) 1964–1965, https://doi.org/10.1007/s11837-014-1136-3.
[11] R.K. Nutor, Q. Cao, X. Wang, D. Zhang, Y. Fang, Y. Zhang, J. Jiang, Phase selection, lattice distortions, and mechanical properties in high-entropy alloys, Adv. Eng. Mater. 2000466 (2020) 1–36, https://doi.org/10.1002/adem.202000466.
[12] B.R. Anne, S. Shaik, M. Tanaka, A. Basu, A crucial review on recent updates of oxidation behavior in high entropy alloys, SN Appl. Sci. 3 (2021) 1–23, https://doi.org/10.1007/s42452-021-04374-1.
[13] J. Lu, G. Ren, Y. Chen, H. Zhang, L. Li, A. Huang, X. Liu, H. Cai, X. Shan, L. Luo, X. Zhang, X. Zhao, Unraveling the oxidation mechanism of an AlCoCrFeNi high-entropy alloy at 1100 °C, Corros. Sci. 209 (2022) 110736, https://doi.org/10.1016/j.corsci.2022.110736.
[14] O.N. Senkov, G.B. Wilks, D.B. Miracle, C.P. Chuang, P.K. Liaw, Refractory high-entropy alloys, Intermetallics 18 (2010) 1758–1765, https://doi.org/10.1016/j.intermet.2010.05.014.
[15] O.N. Senkov, C.F. Woodward, Microstructure and properties of a refractory $NbCrMo_{0.5}Ta_{0.5}TiZr$ alloy, Mater. Sci. Eng. A 529 (2011) 311–320, https://doi.org/10.1016/j.msea.2011.09.033.
[16] F. Xu, X. Gao, H. Cui, Q. Song, R. Chen, Lightweight and high hardness $(AlNbTiVCr)100\text{-}xNi_x$ high entropy alloys reinforced by laves phase, Vacuum 213 (2023) 112115, https://doi.org/10.1016/j.vacuum.2023.112115.
[17] O.S. Bamisaye, N. Maledi, J. Van der Merwe, M.O. Bodunrin, Microstructure, hardness, oxidation and corrosion behavior of Cr(VNb)2 Laves containing CrNbTaVW RHEA in 3.5 wt% NaCl and 1 M H2SO4, Int. J. Refract. Met. Hard Mater. 121 (2024) 106661, https://doi.org/10.1016/j.ijrmhm.2024.106661.

[18] K. Liu, X. Li, J. Wang, Y. Zhang, X. Guo, S. Wu, H. Yu, Investigation of mechanical and corrosion properties of light and high hardness cast AlTiVCrCu$_{0.4}$ high entropy alloy, Mater. Charact. 200 (2023) 112878, https://doi.org/10.1016/j.matchar.2023.112878.

[19] D.G. Kalali, S. Antharam, M. Hasan, P.S. Karthik, P.S. Phani, K. Bhanu Sankara Rao, K.V. Rajulapati, On the origins of ultra-high hardness and strain gradient plasticity in multi-phase nanocrystalline MoNbTaTiW based refractory high-entropy alloy, Mater. Sci. Eng. A 812 (2021) 141098, https://doi.org/10.1016/j.msea.2021.141098.

[20] B. Gorr, S. Schellert, F. Müller, H. Christ, A. Kauffmann, M. Heilmaier, Current status of research on the oxidation behavior of refractory high entropy alloys, Adv. Eng. Mater. 2001047 (2021) 1–14, https://doi.org/10.1002/adem.202001047.

[21] Z. Zhou, X. Peng, W. Lü, S. Yang, H. Li, H. Guo, J. Wang, Ultra-high temperature oxidation resistant refractory high entropy alloys fabricated by laser melting deposition: Al concentration regulation and oxidation mechanism, Corros. Sci. 224 (2023) 111537, https://doi.org/10.1016/j.corsci.2023.111537.

[22] A. Günen, K.M. Döleker, E. Kanca, M.A. Akhtar, K. Patel, S. Mukherjee, Oxidation resistance of aluminized refractory HfNbTaTiZr high entropy alloy, J. Alloys Compd. 999 (2024) 175100, https://doi.org/10.1016/j.jallcom.2024.175100.

[23] T.M. Butler, O.N. Senkov, T.I. Daboiku, M.A. Velez, H.E. Schroader, L.G. Ware, S. Titus, M.S. Titus, Oxidation behaviors of CrNb, CrNbTi, and CrNbTaTi concentrated refractory alloys, Intermetallics 140 (2022) 107374, https://doi.org/10.1016/j.intermet.2021.107374.

[24] Z.S. Nong, Y.N. Lei, J.C. Zhu, Wear and oxidation resistances of AlCrFeNiTi-based high entropy alloys, Intermetallics 101 (2018) 144–151, https://doi.org/10.1016/j.intermet.2018.07.017.

[25] N. Hua, W. Wang, Q. Wang, Y. Ye, S. Lin, L. Zhang, Q. Guo, J. Brechtl, P.K. Liaw, Mechanical, corrosion, and wear properties of biomedical Ti–Zr–Nb–Ta–Mo high entropy alloys, J. Alloys Compd. 861 (2021) 157997, https://doi.org/10.1016/j.jallcom.2020.157997.

[26] X. Pei, Y. Du, T. Li, H. Wang, M. Hu, H. Wang, A combinatorial evaluation of TiZrV$_{0.5}$Nb$_{0.5}$Si$_x$ refractory high entropy alloys: microstructure, mechanical properties, wear and oxidation behaviors, Mater. Charact. 201 (2023) 112956, https://doi.org/10.1016/j.matchar.2023.112956.

[27] J. Li, C. Wang, T. Wang, W. Wang, L. Chai, J. Luo, Oxidation and wear behaviors of MoNbTaW high entropy alloy fabricated via laser energy deposition at elevated temperature, Mater. Charact. 216 (2024) 114221, https://doi.org/10.1016/j.matchar.2024.114221.

[28] V. Bhardwaj, Q. Zhou, F. Zhang, W. Han, Y. Du, K. Hua, H. Wang, Effect of Al addition on the microstructure, mechanical and wear properties of TiZrNbHf refractory high entropy alloys, Tribol. Int. 160 (2021) 107031, https://doi.org/10.1016/j.triboint.2021.107031.

[29] A.D. Akinwekomi, O.S. Bamisaye, M.O. Bodunrin, Powder metallurgy processing of high entropy alloys: bibliometric analysis and systematic review, RAMS 63 (2024) 0188, https://doi.org/10.1515/rams-2023-0188.

[30] S. Zheng, Z. Cai, J. Pu, C. Zeng, L. Wang, Passivation behavior of VAlTiCrSi amorphous high-entropy alloy film with a high corrosion-resistance in artificial sea water, Appl. Surf. Sci. 542 (2021) 148520, https://doi.org/10.1016/j.apsusc.2020.148520.

[31] Y. Gao, K. Chong, L. Qiao, Y. Li, C. Liu, F. Guo, D. Wu, Y. Zou, Synthesis and corrosion behavior of Mo$_{15}$Nb$_{20}$Ta$_{10}$Ti$_{35}$V$_{20}$ refractory high entropy alloy, Mater. Des. 228 (2023) 111820, https://doi.org/10.1016/j.matdes.2023.111820.

[32] K. Chong, Y. Gao, Z. Zhang, Y. Zou, X. Liang, Thermal stability and corrosion behavior of a novel Zr22.5Ti22.5Hf22.5Ni22.5Ta10 high-entropy amorphous alloy, Corros. Sci. 213 (2023) 110979, https://doi.org/10.1016/j.corsci.2023.110979.

[33] Z. Peng, B. Li, Z. Luo, X. Chen, Y. Tang, G. Yang, P. Gong, A lightweight AlCrTiV0.5Cu$_x$ high-entropy alloy with excellent corrosion resistance, Materials 16 (2023) 6072922, https://doi.org/10.3390/ma16072922.

[34] D. Bi, Y. Chang, H. Luo, Z. Pan, Q. Zhao, H. Cheng, X. Wang, C. Qiao, Z. Ni, A. Liu, X. Li, Corrosion behavior and passive film characteristics of AlNbTiZrSi$_x$ high-entropy alloys in simulated seawater environment, Corros. Sci. (2023) 111530, https://doi.org/10.1016/j.corsci.2023.111530.

[35] O.S. Bamisaye, N. Maledi, J. Van der Merwe, D. Klenam, M. Bodunrin, Flow behavior and microstructure of hot-worked TiNbTaVW refractory high-entropy alloy, Adv. Eng. Mater. (2024) 00538, https://doi.org/10.1002/adem.202400538.

[36] O.S. Bamisaye, N. Maledi, J. Van der Merwe, D.E.P. Klenam, M.O. Bodunrin, A. D. Akinwekomi, A comprehensive review on the deformation behavior of refractory high entropy alloys at elevated temperatures, Manuf. Rev. 10 (2023) 1–22, https://doi.org/10.1051/mfreview/2023008.

[37] B. Wang, Q. Wang, N. Lu, X. Liang, B. Shen, Enhanced high-temperature strength of HfNbTaTiZrV refractory high-entropy alloy via Al_2O_3 reinforcement, J. Mater. Sci. Technol. 123 (2022) 191–200, https://doi.org/10.1016/j.jmst.2022.01.025.

[38] O.N. Senkov, S. Gorsse, D.B. Miracle, High temperature strength of refractory complex concentrated alloys, Acta Mater. 175 (2019) 394–405, https://doi.org/10.1016/j.actamat.2019.06.032.

[39] R. Feng, B. Feng, M.C. Gao, C. Zhang, J.C. Neuefeind, J.D. Poplawsky, Y. Ren, K. An, M. Widom, P.K. Liaw, Superior high-temperature strength in a supersaturated refractory high-entropy alloy, Adv. Mater. 33 (2021) 02401, https://doi.org/10.1002/adma.202102401.

[40] Q. Liu, G. Wang, Y. Liu, X. Sui, Y. Chen, S. Luo, Hot deformation behaviors of an ultrafine-grained MoNbTaTiV refractory high-entropy alloy fabricated by powder metallurgy, Mater. Sci. Eng. A 809 (2021) 140922, https://doi.org/10.1016/j.msea.2021.140922.

[41] F. Dong, Y. Yuan, W. Li, Y. Zhang, P.K. Liaw, X. Yuan, H. Huang, Hot deformation behavior and processing maps of an equiatomic MoNbHfZrTi refractory high entropy alloy, Intermetallics 126 (2020) 106921, https://doi.org/10.1016/j.intermet.2020.106921.

[42] B. Wang, H. Zhao, X. Shan, Y. Tang, B. Wang, Y. Tian, Hot deformation behavior and dynamic recrystallization mechanism of Ti$_2$ZrTa$_{0.75}$ refractory complex concentrated alloy, Mater. Charact. 203 (2023) 113061, https://doi.org/10.1016/j.matchar.2023.113061.

[43] K.C. Lo, A.C. Yeh, H. Murakami, Microstructural investigation of oxidized complex refractory high entropy alloys, Mater. Trans. 59 (2018) 556–562, https://doi.org/10.2320/matertrans.MJ201611.

[44] W. Kai, C.C. Liao, I.R. Yang, C.I. Chu, S.F. Liu, J.J. Kai, The oxidation behavior of Ti$_x$(AlCrNb)100−x light-weight medium-entropy alloys in dry air at 600–800 °C, Corros. Sci. 211 (2023) 110890, https://doi.org/10.1016/j.corsci.2022.110890.

[45] L. Ke, L. Meng, S. Fang, C. Lin, M. Tan, T. Qi, High-temperature oxidation behaviors of AlCrTiSi$_{0.2}$ high-entropy alloy doped with rare earth La and Y, Crystals 13 (2023) 1169, https://doi.org/10.3390/cryst13081169.

[46] R. Chen, X. You, K. Ren, Y. Liang, T. Huang, B. Zheng, P. Song, Initial oxidation behavior of AlCoCrFeNi high-entropy coating produced by atmospheric plasma spraying in the range of 650 °C to 1000 °C, Materials 17 (2024) 0550, https://doi.org/10.3390/ma17030550.

[47] S. Schellert, M. Weber, H.J. Christ, C. Wiktor, B. Butz, M.C. Galetz, S. Laube, A. Kauffmann, M. Heilmaier, B. Gorr, Formation of rutile (Cr,Ta,Ti)O$_2$ oxides during oxidation of refractory high entropy alloys in Ta-Mo-Cr-Ti-Al system, Corros. Sci. 211 (2023) 110885, https://doi.org/10.1016/j.corsci.2022.110885.

[48] Y. Yan, K.A. McGarrity, D.J. Delia, C. Fekety, K. Wang, The oxidation-resistance mechanism of WTaNbTiAl refractory high entropy alloy, Corros. Sci. 204 (2022) 110377, https://doi.org/10.1016/j.corsci.2022.110377.

[49] R. Zhu, Y. Yang, B. Zhang, B. Zhang, L. Li, Y. Wu, Z. Mi, Improving mechanical properties and high-temperature oxidation of press hardened steel by adding Cr and Si, Int. J. Miner. Metall. Mater. 31 (2024) 1865–1875, https://doi.org/10.1007/s12613-023-2796-1.

[50] F. Müller, B. Gorr, H.-J. Christ, J. Müller, B. Butz, H. Chen, A. Kauffmann, M. Heilmaier, On the oxidation mechanism of refractory high entropy alloys, Corros. Sci. 159 (2019) 108161, https://doi.org/10.1016/j.corsci.2019.108161.

[51] C. Zhu, X. Li, Z. Ma, Y. Qiao, Z. Zhang, The oxidation behavior of Ti$_{1.5}$NbVAl$_x$ lightweight medium-entropy alloys in dry air at 800°C, Mater. Today Commun. 38 (2024) 108156, https://doi.org/10.1016/j.mtcomm.2024.108156.

[52] Y. Guo, J. Peng, S. Peng, F. An, W. Lu, Z. Li, Improving oxidation resistance of TaMoZrTiAl refractory high entropy alloys via Nb and Si alloying, Corros. Sci. 223 (2023) 111455, https://doi.org/10.1016/j.corsci.2023.111455.

[53] S. Sheikh, M.K. Bijaksana, A. Motallebzadeh, S. Shafeie, A. Lozinko, L. Gan, T. K. Tsao, U. Klement, D. Canadinc, H. Murakami, S. Guo, Accelerated oxidation in ductile refractory high-entropy alloys, Intermetallics 97 (2018) 58–66, https://doi.org/10.1016/j.intermet.2018.04.001.

[54] S. Sheikh, L. Gan, A. Ikeda, H. Murakami, S. Guo, Alloying effect on the oxidation behavior of a ductile Al$_{0.5}$Cr$_{0.25}$Nb$_{0.5}$Ta$_{0.5}$Ti$_{1.5}$ refractory high-entropy alloy, Mater. Today Adv. 7 (2020) 100104, https://doi.org/10.1016/j.mtadv.2020.100104.

[55] R. Zhang, J. Meng, J. Han, K. Tulugan, Oxidation resistance properties of refractory high-entropy alloys with varied Al$_x$CrTiMo content, J. Mater. Sci. 56 (2021) 3551–3561, https://doi.org/10.1007/s10853-020-05480-y.

[56] O.A. Waseem, H.J. Ryu, Combinatorial synthesis and analysis of Al$_x$Ta$_y$V$_z$-Cr$_{20}$Mo$_{20}$Nb$_{20}$Ti$_{20}$Zr$_{10}$ and Al$_{10}$CrMo$_x$NbTiZr$_{10}$ refractory high-entropy alloys: oxidation behavior, J. Alloys Compd. 828 (2020) 154427, https://doi.org/10.1016/j.jallcom.2020.154427.

[57] Z. Shangguan, S. Ma, J. Li, P. Liu, Z. Wang, Study on high-temperature oxidation of TiZrHfNbTaV high-entropy alloy, Mater. Lett. 360 (2024) 135907, https://doi.org/10.1016/j.matlet.2024.135907.

[58] O.S. Bamisaye, N. Maledi, J. Van der Merwe, M.O. Bodunrin, Microstructure, hardness, oxidation, and corrosion behavior of TiNbTaVW refractory high entropy alloy in 3.5 wt% NaCl and 1 M H_2SO_4, J. Alloys Compd. 983 (2024) 173803, https://doi.org/10.1016/j.jallcom.2024.173803.

[59] Y. Lin, Y. Guo, Q. Dong, R. Huang, J. Tan, Effects of vanadium content on the high temperature oxidation behavior of NbTiZrAlV refractory complex concentrated alloys, J. Alloys Compd. 905 (2022) 164180, https://doi.org/10.1016/j.jallcom.2022.164180.

[60] R.N. Nnaji, M.A. Bodude, L.O. Osoba, O.S.I. Fayomi, F.E. Ochulor, Study on high-temperature oxidation kinetics of Haynes 282 and Inconel 718 nickel-based superalloys, Int. J. Adv. Manuf. Technol. 106 (2020) 1149–1160, https://doi.org/10.1007/s00170-019-04290-0.

[61] S. Sheikh, M.K. Bijaksana, A. Motallebzadeh, S. Shafeie, A. Lozinko, L. Gan, T. K. Tsao, U. Klement, D. Canadinc, H. Murakami, S. Guo, Accelerated oxidation in ductile refractory high-entropy alloys, Intermetallics 97 (2018) 58–66, https://doi.org/10.1016/j.intermet.2018.04.001.

[62] B. Gorr, F. Müller, S. Schellert, H.J. Christ, H. Chen, A. Kauffmann, M. Heilmaier, A new strategy to intrinsically protect refractory metal based alloys at ultra high temperatures, Corros. Sci. 166 (2020) 108475, https://doi.org/10.1016/j.corsci.2020.108475.

[63] F. Müller, B. Gorr, H.J. Christ, J. Müller, B. Butz, H. Chen, A. Kauffmann, M. Heilmaier, On the oxidation mechanism of refractory high entropy alloys, Corros. Sci. 159 (2019) 108161, https://doi.org/10.1016/j.corsci.2019.108161.

[64] H. Chen, A. Kauffmann, B. Gorr, D. Schliephake, C. Seemüller, J.N. Wagner, H. J. Christ, M. Heilmaier, Microstructure and mechanical properties at elevated temperatures of a new Al-containing refractory high-entropy alloy Nb-Mo-Cr-Ti-Al, J. Alloys Compd. 661 (2016) 206–215, https://doi.org/10.1016/j.jallcom.2015.11.050.

[65] F. Müller, B. Gorr, H.J. Christ, H. Chen, A. Kauffmann, M. Heilmaier, Effect of microalloying with silicon on high temperature oxidation resistance of novel refractory high-entropy alloy ta-Mo-Cr-Ti-Al, Mater. High Temp. 35 (2018) 168–176, https://doi.org/10.1080/09603409.2017.1389115.
[66] J. Jayaraj, P. Thirathipviwat, J. Han, A. Gebert, Microstructure, mechanical and thermal oxidation behavior of AlNbTiZr high entropy alloy, Intermetallics 100 (2018) 9–19, https://doi.org/10.1016/j.intermet.2018.05.015.
[67] C. Xu, L. Fang, G. Xu, L. Yang, Y. Ouyang, X. Tao, Mechanical properties and oxidation behavior of NbMoTaWx refractory high entropy alloys, J. Alloys Compd. 990 (2024) 174390, https://doi.org/10.1016/j.jallcom.2024.174390.
[68] L. Chen, Z. Yang, L. Lu, X. Zhang, X. Ren, Effect of TiC on the high-temperature oxidation behavior of WMoTaNbV refractory high entropy alloy fabricated by selective laser melting, Int. J. Refract. Met. Hard Mater. 110 (2023) 106027, https://doi.org/10.1016/j.ijrmhm.2022.106027.
[69] X. Pei, Y. Du, H. Wang, T. Li, M. Hu, H. Wang, W. Liu, Effects of Al/Si on the oxidation behavior of a $TiZrV_{0.5}Nb_{0.5}$ refractory high entropy alloy at 1000 °C, Corros. Sci. 224 (2023) 111527, https://doi.org/10.1016/j.corsci.2023.111527.
[70] Y. Xiao, W. Kuang, Y. Xu, L. Wu, W. Gong, J. Qian, Q. Zhang, Y. He, Microstructure and oxidation behavior of the CrMoNbTaV high-entropy alloy, J. Mater. Res. 34 (2019) 301–308, https://doi.org/10.1557/jmr.2018.340.
[71] H. Jahangiri, S. Mohagheghi, A. Asghari Alamdari, K. Gürcan Bayrak, E. Ayas, U. Ünal, A. Motallebzadeh, High temperature oxidation behavior of the AlCrFeMnTi light-weight high-entropy alloy, ACS Appl. Eng. Mater. 1 (2023) 1766–1774, https://doi.org/10.1021/acsaenm.3c00161.
[72] H. Jeong, S.H. Kim, W.S. Choi, P.P. Choi, Spallation resistance of oxide scales on alloy 617 enhanced by boron addition, Corros. Sci. 140 (2018) 196–204, https://doi.org/10.1016/j.corsci.2018.06.002.
[73] R. Su, H. Zhang, G. Ouyang, L. Liu, D.D. Johnson, J.H. Perepezko, Oxidation mechanism in a refractory multiple-principal-element alloy at high temperature, Acta Mater. 246 (2023) 118719, https://doi.org/10.1016/j.actamat.2023.118719.
[74] X. Zhang, X. Cui, G. Jin, Y. Dong, Z. Wang, Y. Qi, Microstructure evolution and performance enhancement of NbTaTiV-(Cr, Zr, W) single-phase refractory high-entropy alloy coatings: role of additional elements, J. Alloys Compd. 951 (2023) 169918, https://doi.org/10.1016/j.jallcom.2023.169918.
[75] B.M. Hunter, A., Oxidation Behavior of Refractory Complex Concentrated Alloys: Computational and Experimental Studies, Thesis, University of Alabama, 2019.
[76] L. Zheng, M.C. Zhang, R. Chellali, H. Bouchikhaoui, J.X. Dong, Oxidation property of powder metallurgy EP741NP Ni based superalloy at elevated temperatures, Mater. Technol. 28 (2013) 122–128, https://doi.org/10.1179/1753555712Y.0000000030.
[77] Y.Z. Wang, N. Gao, X.W. Liu, W.M. Chen, H.T. Zheng, The oxidation behavior of a ductile $Hf_{0.5}Nb_{0.5}Ta_{0.5}Ti_{1.5}Zr$ refractory high-entropy alloy in pure oxygen condition at 500–900 °C, J. Mater. Res. Technol. 25 (2023) 5457–5468, https://doi.org/10.1016/j.jmrt.2023.07.003.
[78] W. Kuang, G.S. Was, A high-resolution characterization of the initiation of stress corrosion crack in alloy 690 in simulated pressurized water reactor primary water, Corros. Sci. 163 (2020) 108243, https://doi.org/10.1016/j.corsci.2019.108243.
[79] J. Kuang, P. Zhang, Q. Wang, Z. Hu, X. Liang, B. Shen, Formation and oxidation behavior of refractory high-entropy silicide $(NbMoTaW)Si_2$ coating, Corros. Sci. 198 (2022) 110134, https://doi.org/10.1016/j.corsci.2022.110134.
[80] U. Jain, J. Sonber, R. Tewari, High temperature oxidation behaviour of V-Ti-ta alloys, Fusion Eng. Des. 144 (2019) 125–132, https://doi.org/10.1016/j.fusengdes.2019.04.070.
[81] N. Esparza, V. Rangel, A. Gutierrez, B. Arellano, S.K. Varma, A comparison of the effect of Cr and Al additions on the oxidation behaviour of alloys from the Nb-Cr-Si system, Mater. High Temp. 33 (2016) 105–114, https://doi.org/10.1179/1878641315Y.0000000012.
[82] R. Mevrel, Cyclic oxidation of high-temperature alloys, Mater. Sci. Technol. 3 (1986) 531–535, https://doi.org/10.1080/02670836.1987.11782264.
[83] C.A. Barrett, Effect of 0.1 at.% zirconium on the cyclic oxidation resistance of beta-NiAI, Oxid. Met. 30 (1988) 5–6, https://doi.org/10.1007/BF00659006.
[84] C.A. Barrett, R.V. Miner, D.R. Hull, The effects of Cr, AI, Ti, Mo, W, Ta, and Cb on the cyclic oxidation behavior of cast Ni-base superalloys at 1100 and 1150°C, Oxid. Met. 20 (1983) 256–278.
[85] E.A. Basuki, N. Adrianto, R. Triastomo, A.A. Korda, T.L. Achmad, F. Muhammad, D.H. Prajitno, Isothermal oxidation behavior of ferritic oxide dispersion strengthened alloy at high temperatures, J. Eng. Technol. Sci. 54 (2022) 370–382, https://doi.org/10.5614/j.eng.technol.sci.2022.54.2.10.
[86] B. Gwalani, A. Martin, E. Kautz, B. Guo, S.V. Lambeets, M. Olszta, A.K. Battu, A. Malakar, F. Yang, J. Guo, S. Thevuthasan, R. Li, A. Amassian, M. Thuo, A. Devaraj, Mechanistic understanding of speciated oxide growth in high entropy alloys, Nat. Commun. 15 (2024) 5026, https://doi.org/10.1038/s41467-024-49243-8.
[87] L. Qin, P. Ren, Y. Yi, T. Xie, Y. Hu, D. Chen, S. Zhou, Effect of Al_2O_3 content on the high-temperature oxidation behaviour of CoCrAlYTa coatings produced by laser-induction hybrid cladding, Corros. Sci. 209 (2022) 110739, https://doi.org/10.1016/j.corsci.2022.110739.
[88] N. Yurchenko, E. Panina, S. Zherebtsov, G. Salishchev, N. Stepanov, Oxidation behavior of refractory $AlNbTiVZr_{0.25}$ high-entropy alloy, Materials 11 (2018) 2526, https://doi.org/10.3390/ma11122526.